Combustion and Flame 238 (2022) 111898

Contents lists available at ScienceDirect

Combustion and Flame

journal homepage: www.elsevier.com/locate/combustflame

Rapid change of particle velocity due to volatile gas release during biomass devolatilization

Ángel David García Llamas[a,*], Ning Guo[b], Tian Li[b,c], Rikard Gebart[a], Kentaro Umeki[a]

[a] Energy Engineering, Division of Energy Science, Luleå University of Technology, Luleå, Sweden
[b] Department of Energy and Process Engineering, Faculty of Engineering, NTNU - Norwegian University of Science and Technology, Trondheim, Norway
[c] RISE Fire Research, Tiller 7092, Norway

ARTICLE INFO

Article history:
Received 14 July 2021
Revised 17 November 2021
Accepted 18 November 2021
Available online 21 December 2021

Keywords:
Biomass devolatilization
TR-PTV
In-situ measurements
Rocket effect
Non-isothermal modelling

ABSTRACT

Our earlier study showed significant differences in average particle velocity between simulation and experimental results for devolatilizing biomass particles in an idealised entrained flow reactor [N. Guo et al., Fuel, 2020]. This indicates that the simulations do not accurately describe the physicochemical transformations and fluid dynamic processes during devolatilization. This article investigates the reasons for these discrepancies using time-resolved analyses of the experimental data and complementary modelling work. The experiments were conducted in a downdraft drop-tube furnace with optical access, which uses a fuel-rich flat flame (CH_4–O_2–CO_2) to heat the particles. Gas flow was characterized using particle image velocimetry, equilibrium calculations and thermocouple measurements. High-speed images of devolatilizing Norway spruce (*Picea Abies*) particles were captured and analysed using time-resolved particle tracking velocimetry methods. The data were used to estimate the balance of forces and fuel conversion. Thrust and "rocket-like" motions were frequently observed, followed by quick entrainment in the gas flow. Rocketing particles were, on average, smaller, more spherical and converted faster than their non-rocketing counterparts. These differences in conversion behaviour could be captured by a particle-size dependent, 0-D devolatilization model, corrected for non-isothermal effects. The results from this investigation can provide a basis for future modelling and simulation work relevant for pulverized firing technologies.

1. Introduction

The benefits of biomass as a CO_2-neutral energy source [1] have led to a renewed interest in industrial applications during the last decades to mitigate the global warming problem [2,3]. Biomass fuels are compatible with existing large-scale energy conversion technologies, such as pulverized suspension firing. Suspension firing is also relevant in biofuel production technologies, such as entrained flow gasification, and technologies for CO_2 emission reduction, such as oxy-fuel combustion [4,5]. However, the unique properties of biomass, e.g. much higher reactivity, non-spherical particle morphology, and different ash composition than fossil fuels, create a need for further investigation before they can be implemented on a global scale [6].

During suspension firing, particles undergo a rapid conversion that can be separated into the following three stages: drying, devolatilization, and char gasification/combustion [7]. The conversion behaviour depends on the heating rate, peak temperature, residence time at high temperature and the local gas concentration around the particle. During devolatilization, the particles undergo significant morphological transformations and release more than 70% of their initial mass in the form of vapour and gases [8]. This is an intensely heat-driven process, which is promoted by high heating rates [9]. However, the apparent rate can be restricted by blowing [10], evaporative cooling [11], endothermicity of reactions [12] and internal convective flow of volatiles [13], which takes place preferentially in the direction of the pores [14], usually aligned with the longest dimension. In addition, biomass particles tend to be elongated rather than spherical, which affects heat transfer [14]. All these heat transfer resistances make the particles non-isothermal during the devolatilization stage for a wide range of fuel size fractions under industrially realistic conditions for suspension firing. However, computational fluid dynamics (CFD) simulations generally consider particles to be thermally thin, such as below 100 µm of equivalent spherical diameter [15] and especially at very high heating rates [11]. Apparent devolatiliza-

* Corresponding author at: Lulea University of Technology: Lulea Tekniska Universitet, Sweden.
E-mail address: anggar@ltu.se (Á.D.G. Llamas).

https://doi.org/10.1016/j.combustflame.2021.111898

Nomenclature

A:	area, m^2
AR:	aspect ratio, max./min. Dimension, -
B:	blowing coefficient, -
C:	specific heat, $J•kg^{-1}•K^{-1}$
C_d:	drag coefficient, -
d:	diameter, m
e:	unit vector
E_r:	energy emitted by radiation, J
F:	force, N
L_v:	latent heat of vaporization, $J•kg^{-1}$
m:	mass, kg
Nu:	Nusselt number, -
Pr:	Prandtl number, -
q:	yield, $kg•s^{-1}$
Re:	Reynolds number, -
T:	temperature, K
t:	time, s
v:	velocity, $m•s^{-1}$
V:	volume, m^3

Greek letters

α:	Absorptivity
ΔH:	endothermic heat of reaction, $J•kg^{-1}$
ε:	Emissivity, -
μ:	dynamic viscosity, Pa•s
ν:	kinematic viscosity, $m^2•s^{-1}$
ρ:	density, $kg•m^{-3}$
σ_{SB}:	Boltzmann constant, $5.6703•10^{-8}$, $W•m^{-2}•K^{-4}$
Ω:	Solid angle, sr

Subscripts

B:	Basset force, N
D:	drag force, N
eff:	effective
eq:	equivalent for a sphere with the same volume
f:	film
g:	gas
L:	lift force, N
p:	particle
P:	pressure, Pa
r:	ratio
sf:	Stefan
T:	thrust force, N
VM:	virtual mass, kg
vol:	volatiles

tion kinetics models for high heating rates must account for non-isothermal particles, such as in the model developed by Johansen et al. [9,15,16], which simplifies the non-isothermal problem by providing apparent devolatilization kinetics parameters for different size fractions.

The advection of devolatilization products from the particle also affects the gas velocity field and viscosity around the particle, potentially influencing viscous and pressure forces [17]. Momentum exchange can also cause thrust if blowing is directional. In fact, sudden acceleration has been observed during the fast devolatilization of biomass due to directional gas ejection [18]. This has been related to heterogeneous heating and preferential gas advection through the anisotropic pore structures of the particle [19]. Following this line of thought, Elfasakhany et al. [18] and our previous work [20] modelled this phenomenon as a thrust force caused by a heterogeneous release of volatiles, in a phenomenon referred here as "rocketing". An alternative explanation, based on experimental observations of cellulose particles undergoing reactive boiling [21], could be the presence of an intermediate molten phase that forms a bubble with a high internal pressure that suddenly bursts and releases the enclosed pyrolysis products. Under this assumption, the devolatilization model developed by Montoya et al. [22] includes bubble formation, coalescence, and rising in the molten phase to explain these bursts of gas. Further evidence for this latter mechanism is supported by the inspection of particles that had undergone devolatilization. Fig. 1 shows SEM images of Norway Spruce particles and their char, obtained in a drop tube furnace under pyrolysis conditions at 1200 °C. Fig. 1b depicts that particles formed spherical, hollow char structures (cenospheres) with distinct holes on the surface due to melting [23,24]. The presence of these holes in the molten char structures is common for various biomass species [24,25] and indicates the violent bubbling and boiling processes during the melting process. It is possible that if melting occurred, volatile gases could have escaped through these holes, causing thrust. Additionally, experiments performed by Riaza et al. [26] showed that elongated particles tend to heat up heterogeneously, more intensely in the edges. Under such circumstances, localised melting could close the pores and produce microexplosions under very high heating rates ($>10^5$ K/s).

Despite the pile of evidence, volatile-driven momentum exchange between particles and bulk gas flow is usually disregarded in simulation models since it is assumed to occur homogeneously in all directions, therefore cancelling out thrust forces. In addition, not much has been investigated experimentally about the relevance, mechanisms and implications of the "rocketing" phenomenon under industrially realistic conditions, using *in-situ* measurements. Disregarding these forces can potentially lead to inaccurate estimations of particle residence time, which is crucial when modelling industrial burners. Furthermore, the non-isothermal behaviour, blowing effects on heat transfer, unsteady forces, morphological and density changes, etc., are often disregarded in CFD simulations to reduce computational time and reduce model complexity without significant experimental evidence.

There is a lack of experimental measurements of the "rocketing" phenomenon for streams of biomass particles under devolatilization, especially with respect to its relevance, predictability, and relationship to the heterogeneous blowing. In this work, we describe the "rocketing" phenomenon during biomass devolatilization and investigate its relevance by estimating its frequency within a stream of devolatilizing particles. We provide a simple statistical predictive model based on particle size and shape, valid for the studied experimental conditions. In addition, we estimate the mass and magnitude of the forces on a "rocketing" particle during devolatilization with the aid of existing models which capture the complex heat and mass transfer effects and the thrust force from experimental data.

2. Methodology

A schematic of the experimental apparatus can be seen in Fig. 2. The reactor is a drop-tube setup with optical access. A supporting flame supplies the heat and reaction environment to the devolatilizing particles. The combustion products of the supporting flame were chosen to achieve a similar composition to the one found in the near-burner zone of entrained-flow gasifiers and oxy-fuel burners. The supporting flat flame was produced by the fuel-rich combustion of $CH_4/CO_2/O_2$, whose products were mainly $H_2/CO_2/CO/H_2O$ and free of oxygen. Compositions of post-combustion gas were measured using gas chromatography and detailed in Table S2 in the supplementary material. The biomass particles were injected from a central tube with a stream of CO_2 gas at a feeding rate of approximately 10 $g•h^{-1}$. The feedstock used

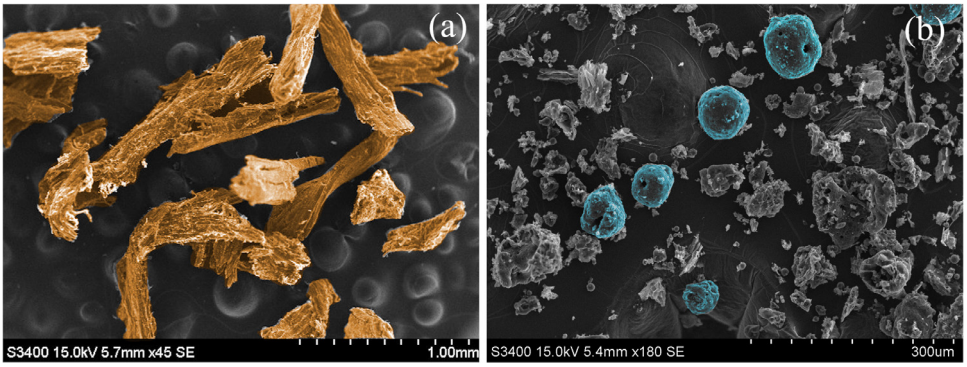

Fig. 1. SEM images of Norwegian Spruce char particles from high temperature (1200 °C) pyrolysis experiments in a drop tube furnace, (a) typical particles before heating, highlighted in brown, (b) cenospheres formed during heating, highlighted in blue. Notice the holes in the cenospheres. Adopted from [26] with permission from ACS.

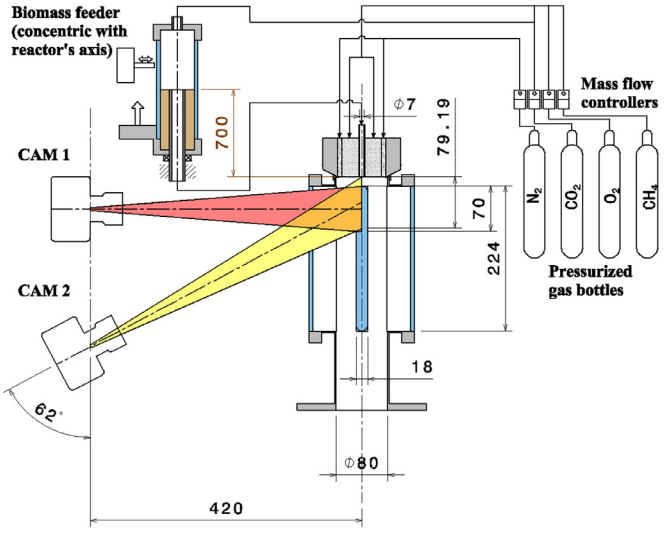

Fig. 2. Schematic representation of the reactor setup, all measurements are in mm. Reprinted from [28], with permission from Elsevier.

was Norwegian spruce particles (*Picea Abies*) produced by a hammer mill followed by sieving with a sieve size of 200–250 µm. The resulting particles had a high aspect ratio (AR=3.9 ± 2.9, defined as the ratio of longest to shortest diameter). Fuel properties and reaction conditions for the supporting flame and carrier gases can be seen in Tables S1 and S2 in the supplementary material. Imaging was performed by two high-speed cameras, which collected the scattered light of a pulsed-laser sheet that shone across the stream of particles and the reactor's axis. Images were sampled at 800 Hz with an exposure time of 625 µs during 3.75 s, for a field of view of 20 × 74 mm. The cylindrical lens for the laser optics was placed approximately 1.5 m from the reactor's axis, well below the flat flame burner. This arrangement was made in order to take advantage of the dispersion angle of the laser, so as to illuminate the particles entering the reactor (See Section 1 of the supplementary material for further schematics). The minimum spatial resolution of the imaging system was 53.9 µm. Dynamic Studio 6.8 from Dantec Dynamics and Matlab were used to collect and post-process the images in order to obtain time-resolved measurements of velocity, position and dimensions of the particles. The reader is referred to [27,28] for more details about the experimental conditions, setup description and methodology used for image processing.

Gas velocity without particles was measured using particle image velocimetry (PIV), seeding the carrier gas flow with titanium dioxide particles. The same arrangement and software used for particle tracking velocimetry (PTV) were also used for the PIV measurements. In this study, the particle slip velocity is defined as the difference between the velocity of the gas flow at the particle position measured without particles and the instantaneous particle velocity. This approximation seems adequate since the volume fraction is below 10^{-4}, and therefore the flow can be considered dilute, with negligible effects of the particles on the gas velocity field [29]. Additionally, measurements of gas flow velocity without particles indicate that the gas flow is laminar, and time oscillations can be disregarded (see Section 4 of the supplementary material). There are methods to perform simultaneous measurements of gas and particle velocity, with a combination of PIV and PTV, such as the one described by Khalitov and Longmire [30]. However, such methods were not considered in this study because the simultaneous measurement of gas and particle velocity would have required additional seeding particles, possibly obstructing the performance of the current methodology for volatile cloud edge detection. Additionally, gas seeding would have affected the radiative properties of the gas due to the incandescence of the seeding particles, as well as acting as a heat ballast. Statistics for gas measurements without particles are provided in Section 4 of the supplementary material.

A flow scheme with the methodology for data analysis and modelling for this work is presented in Fig. 3. In this chart, the central sequence of data treatment corresponds to retrieving information from TR-PTV data. This information was used to deduce a time-averaged, statistical regression model to predict the probability of "rocketing" (sequence to the right). Additionally, modelling was carried out using the experimental data of selected particles (sequence to the left). Further explanation of the models used can be found in subsequent sections.

It should be noted that this experimental study cannot track particle rotation since it is not based on volumetric imaging. With this setup, only the projected area of the particle can be accounted for. Rotation produces oscillatory effects in the minimum and maximum dimensions of the projected area. If the number of samples is high enough, and the sampling rate is higher than the particle rotation, the average measurements of minimum and maximum dimensions should correspond to the real ones. This procedure is similar to the one applied by commercially available tools, such as shadowgraph particle-size analysers.

However, time-resolved measurements can be biased by particle rotation. Fortunately, these oscillations can be compensated by filtering to capture the general trends. For the time-resolved study included in this work, particles showing small oscillations due to rotation were selected. Other more sophisticated techniques, such as machine learning can be used to predict 3D rotation from planar measurements.

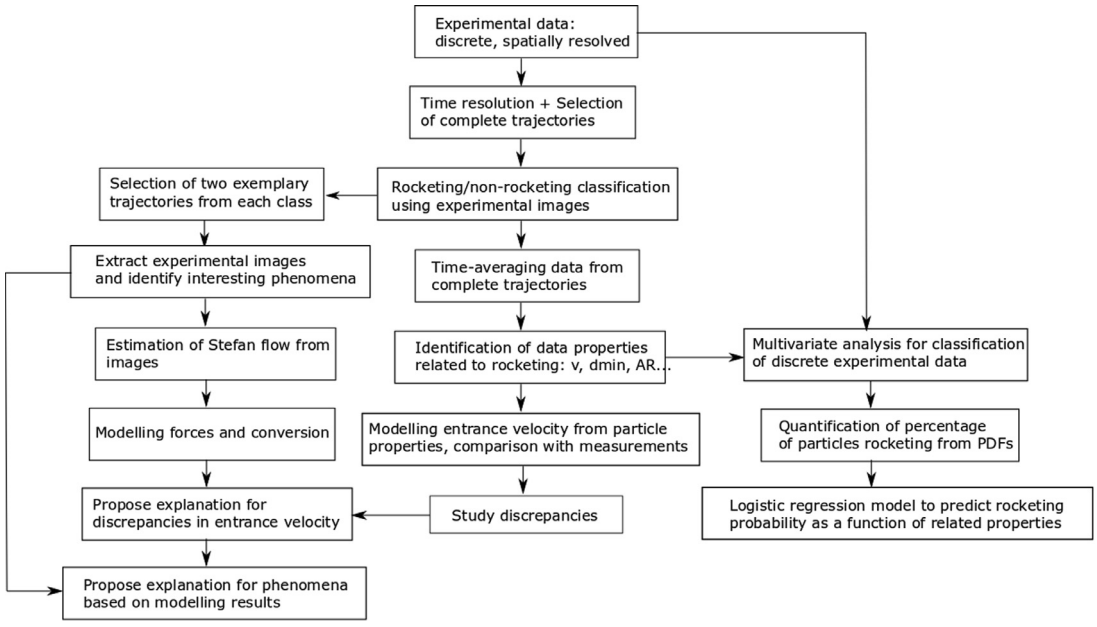

Fig. 3. Flow chart with the process for data analysis performed in this work.

2.1. Estimation of particle mass during devolatilization from experimental measurements and estimated forces

The particle mass was estimated from experimental data based on momentum conservation during devolatilization. The objective is to provide an estimate of the mass loss during "rocketing", along with the thrust force which could explain this phenomenon. Eq. (1) expresses the transient motion of a devolatilizing particle immersed in a gas flow [29]:

$$\vec{F}_B + \vec{F}_D + \vec{F}_L + \vec{F}_P + \vec{F}_{VM} + m_p g\vec{j} + \vec{F}_T = m_p \frac{d\vec{v}_p}{dt} \tag{1}$$

The unit vector $\vec{j}$ represents the direction of gravity. The origin of coordinates can be seen in Fig. 4, and particle movement is assumed to occur within the plane defined by the x and y-axis, without out-of-plane movements. This was possible since there was a sufficient number of particles not exhibiting out of plane movements (around 80% of the incoming particles). More information about out-of-plane movements can be found in Section 6 of the supplementary material. A schematic representation of the dominant forces on the particle (drag, weight, inertia and thrust) is depicted in Fig. 4. The forces are estimated from available models in the literature (Table 1), using the spatial field of gas properties at each particle position and time-resolved particle properties (velocity, diameter, etc.). Thrust force is dependent on the mass loss and requires the estimation of the Stefan flow from the particle surface. Fig. 4 also shows a schematic representation of a cloud of volatile products being expelled from the particle with a heterogeneous Stefan flow, in this case with a higher velocity of the expelled gases in the leeward direction. The local Stefan flow velocity of devolatilization products at the particle surface is identified as $\vec{v}_{sf}$. Due to the heterogeneity of the Stefan flow field, its integral across a surface enclosing the particle is non-zero and equivalent to a resultant velocity. This consequent velocity has been named thereafter "effective velocity", $\vec{v}_{eff}$, as it is commonly referred to in propulsion theory:

$$\vec{v}_{eff} = \oint \frac{\vec{v}_{sf}}{r^2} \cdot d\vec{S} = \oint \vec{v}_{sf} \cdot d\Omega \tag{2}$$

This effective velocity is assumed to be the cause for the thrust force F_T:

$$\vec{F}_T = \frac{dm_p}{dt}\vec{v}_{eff} \tag{3}$$

Propagation of uncertainty in the calculation of the solution for $m(t)$ can be minimized by projecting all terms of Eq. (1) in the direction of the acceleration. This is because the horizontal component of particle velocity is usually close to zero and, therefore, its differentiation carries high experimental uncertainty. Including the definition of thrust force from Eq. (3) into Eq. (1), and multiplying by the unit vector parallel to the acceleration, the resulting equation becomes:

$$\left(\vec{F}_B + \vec{F}_D + \vec{F}_L + \vec{F}_P + \vec{F}_{VM} + m_p g\vec{j} + \frac{dm_p}{dt}\vec{v}_{eff}\right) \cdot \vec{e}_a = m_p \frac{d\vec{v}_p}{dt} \cdot \vec{e}_a \tag{4}$$

where $\vec{e}_a = \frac{d\vec{v}_p}{dt} / \left|\frac{d\vec{v}_p}{dt}\right|$ is the unit vector in the direction of the acceleration. Eq. (4) is a first-order ordinary differential equation for the particle mass, which can be solved numerically under the condition that all the forces and other unknowns can be estimated from the experimental data. The particle mass was calculated numerically, using a variable-step, variable-order (VSVO) solver, suitable for stiff ODEs, using the Matlab function "ode15s" for version R2021a [31]. The initial density of the particle was assumed to be 440 kg/m^3 [32]. Tsiolkovski's "Ideal rocket" equation [33] was used to check whether the mass loss during "rocketing" can explain the observed change of momentum that is unaccounted for by the rest of the forces (see Section 2.1.2).

2.1.1. Estimation of the Stefan velocity and the effective velocity from recorded images

The Stefan flow field emanating from the surface of the particle can be estimated from the expansion of the cloud of incandescent matter that surrounds the particle under pyrolysis conditions. The camera sensor was able to capture the light from the incandescent sooty cloud in the absence of laser illumination, indicating that it resulted from the combination of integrated emission along the optical path and cross-sectional scattering from the laser sheet. This estimation can only be accurate as long as the particle moves

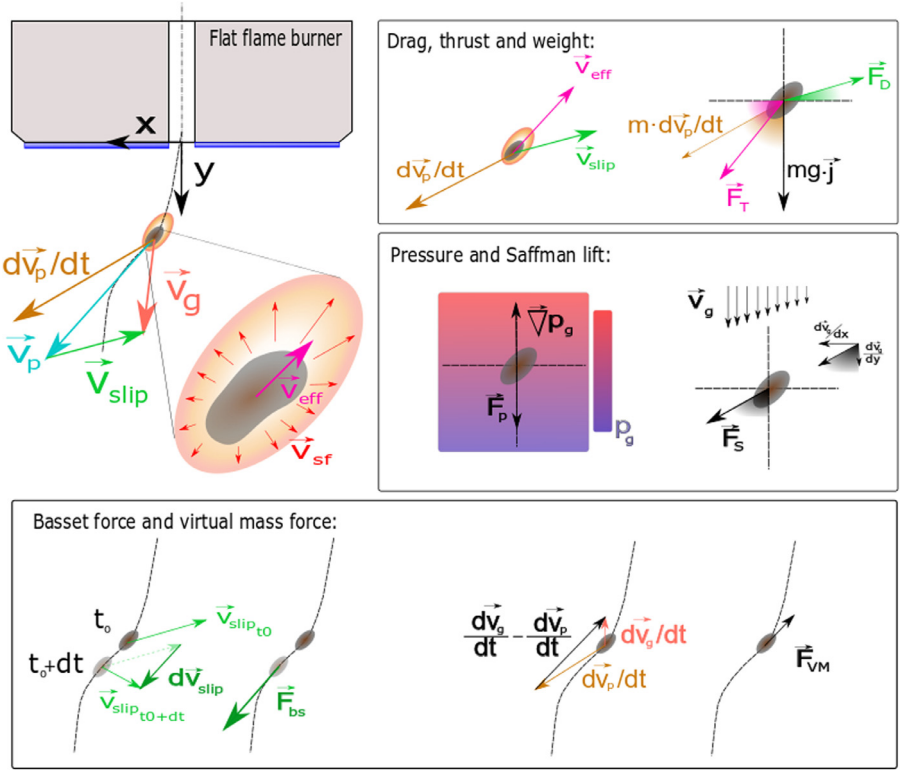

Fig. 4. Representation of the main forces on the particle.

Table 1
Summary of models used to calculate forces.

Equation	Description	References
$\vec{F}_D = \frac{1}{2}\rho_g C_d C_{d,r} A_p \lvert\vec{v}_{slip}\rvert \vec{v}_{slip}$	Drag force	[29]
With:	Drag coefficient according to	[29]
$C_d = \frac{24}{Re}(1 + 0.15Re^{0.687})$	Schiller-Naumann correlation	[32]
And:	Drag ratio for a prolate spheroid with random orientation: Clift correction.	
$C_{d,r} = \frac{\bar{c}}{6\pi d_{eq}}$		
$\bar{c} = \frac{6\pi d_{eq}\sqrt{AR^2-1}}{\ln(AR+\sqrt{AR^2-1})}$		
$F_B = \frac{9}{d_{eq}}\alpha_d\sqrt{\frac{\rho_g \mu_g}{\pi}}\int_0^t \frac{\frac{dv_{slip}}{dt}}{\sqrt{t-\tau_s}}dt$	Basset force	[33]
With:		
$\tau_s = \frac{\rho_p d_{eq}^2}{18\mu_g}$		
$\vec{F}_{VM} = \frac{M_f}{2}\left(\frac{D\vec{v}_g}{Dt} - \frac{d\vec{v}_p}{dt}\right)$	Virtual mass force	[33]
M_f is the mass of fluid displaced by the particle, calculated using the equivalent diameter, d_{eq} and the local gas density ρ_g		
$\vec{F}_P = -V_{eq}\cdot\vec{\nabla}p$	Pressure-gradient force	[34]
V_{eq} is the displaced volume of gas by the particle, calculated using the equivalent diameter, d_{eq}.		
$\vec{F}_L = \vec{F}_S = 1.61\mu_g d_{eq}\lvert v_{slip}\rvert(\sqrt{Re_{G,x}}\cdot\vec{i} + \sqrt{Re_{G,y}}\cdot\vec{j})$	Saffman lift force	[35]
With:		
$Re_{G,x} = \frac{d_{eq}^2\cdot(\frac{dv_{g,x}}{dx} + \frac{dv_{g,y}}{dx})}{v_g}$		
$Re_{G,y} = \frac{d_{eq}^2\cdot(\frac{dv_{g,x}}{dy} + \frac{dv_{g,y}}{dy})}{v_g}$		

within a 2D plane, turbulence is low and volatile matter is heated up enough to become incandescent. Consequently, this method is only applicable to those particles that do not move out of the thin laser sheet used for particle detection. The method consists of applying an edge filter to raw images to detect the edge of the cloud of volatiles. Afterwards, the Stefan flow velocity can be calculated from the expansion of the edge, relative to the particle centroid, between consecutive frames. A scheme of such a process is shown in Fig. 5.

If the Stefan flow velocity is assumed to emanate radially from the particle centroid, its local value can be expressed as a function of θ, which is the angle formed with the vertical axis:

$$\vec{v}_{sf}(\theta) = \frac{L}{\Delta t}\frac{1}{\theta}\,\vec{e}_\theta \tag{5}$$

Using Eq. (2), $\vec{v}_{sf}(\theta)$ can be used to calculate $\vec{v}_{eff}$, as in Eq. (6):

$$\vec{v}_{eff} = \oint \vec{v}_{sf}(\theta)\cdot\vec{e}_\theta\, d\theta \tag{6}$$

The methodology here presented is only applicable under laminar conditions for small particle Reynolds numbers. These conditions differ significantly from those found under realistic indus-

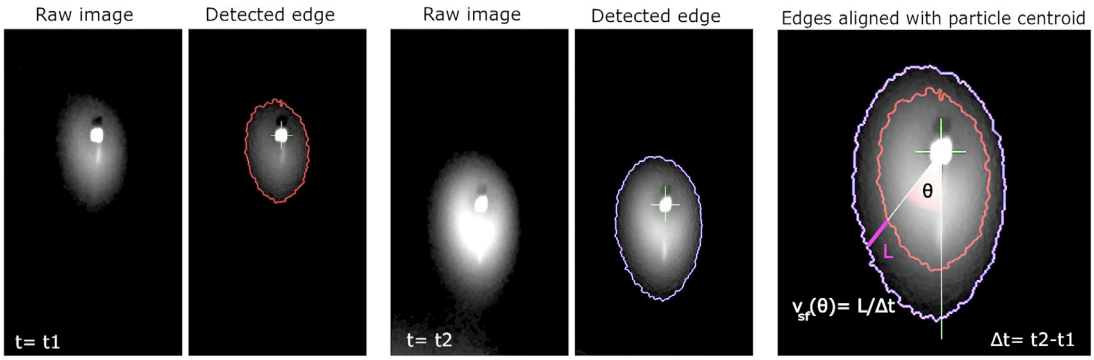

Fig. 5. Estimation of Stefan flow velocity from edge detection of the incandescent cloud of volatiles around the particle. Green crosses identify the particle centroid. These images and edges have been obtained from real experimental data, with Δt=3 ms between t1 and t2, using a Sobel filter for edge detection. Contrast has been adjusted for easier visualization.

trial pulverized burners, such as entrained-flow gasification. However, the applicability for industrially-realistic conditions would be more plausible with a similar methodology to the one proposed, involving stereoscopic measurements on an electrodynamic thermogravimetric analyser. This would enable very high heating rate, controlled atmosphere and simultaneous visualisation, such as in the work by E. Bar-Ziv et al. [34] and the more recent by Biagini et al. [35], in combination with powerful tools for the measurement of volatile gas velocity out of the particle, such as interferometry, as it was performed by Lycksam et al. [36] or LIF (Laser Induced Fluorescence).

2.1.2. The ideal rocket equation

To check whether the velocity changes experienced by a particle can be explained by the mass estimated as described above, the equation for the movement of an ideal rocket without drag is used for comparison. This equation was described by Tsiolkovski [33], and relates the change of velocity of the ideal rocket with the "effective velocity" of the propelled gases and the change of mass during this process:

$$\Delta v_p = v_{eff} \cdot \ln\left(\frac{m_0}{m_f}\right) \tag{15}$$

where Δv_p is the increase in velocity of the rocket (in this case, the particle), v_{eff} is the effective velocity of the gases propelled out of the rocket (volatiles) and $\frac{m_0}{m_f}$ is the ratio of initial to final mass of the rocket.

2.2. Estimation of particle conversion from experimental data and non-isothermal devolatilization models

Conversion of a biomass particle during devolatilization was estimated, considering the effect of changes in particle size and shape as well as gas temperature on heat transfer. Non-isothermal heating and blowing effects were also taken into account. The aim was to find out which model reproduces the estimated mass loss obtained from momentum conservation more accurately (Section 2.1), and to provide an estimate of the heating rate and product composition during conversion of a "rocketing" particle. The spatial field of gas properties and time-resolved particle dimensions were used to estimate the time-dependent heat transfer rate by convection and radiation from available models, using the energy conservation equation. The obtained particle temperature is then used to update the kinetic parameters of a 0D conversion model, taking into account non-isothermal heating.

Particle temperature is calculated for each experimental point from the energy conservation equation:

$$m_p C_p \frac{dT_p}{dt} = -hA_p(T_p - T_g) - E_r + q_{vol}\Delta H_{vol} \tag{16}$$

In this equation, particle mass and particle temperature can be obtained from the simultaneous solution of the chemical kinetics of Table 2 and Eq. (16). Thermochemical gas properties were obtained from interpolation from temperature measurements from the NIST Chemical Kinetics Database [37]. The heat of devolatilization, ΔH_{vol}, was obtained from [10]. Initial density of the particle was assumed as 440 kg/m^3 [32] and the initial temperature of the particle was assumed to be 300 K.

External convective heat transport is usually modelled using heat transfer correlations for spheres using a Nusselt number correlation (Nu=hD/λ). One common correlation is that of Ranz-Marshall [38]:

$$Nu = 2 + 0.6Re^{\frac{1}{2}}\mathrm{Pr}^{\frac{1}{3}} \tag{17}$$

where thermochemical properties at film condition are used to calculate Reynolds and Prandtl numbers. However, the presence of an outflow of devolatilization products from the particle surface must be taken into account with a correction to the estimation of the film temperature, using the 1/3 rule, as suggested by Yuen and Chen [17]:

$$T_f = T_p + \frac{T_g - T_p}{3} \tag{18}$$

To account for blowing effects, several authors suggest a Nusselt number correction based on a blowing coefficient (also called mass transfer ratio or Spalding heat transfer number) [10,38,39]. The Nusselt number correction from the heat transfer number can be obtained from the model developed by Renksizbulut & Yuen, correcting the Ranz-Marshall correlation from Eq. (17):

$$Nu_r = \frac{Nu}{(1+B)^{0.7}} \tag{19}$$

where B is the blowing coefficient, calculated as:

$$B = \frac{C_p(T_p - T_g)}{L_v} \tag{20}$$

where L_v is the latent heat of vaporization of a liquid droplet, which can be approximated by using Trouton's rule for the boiling temperature of the molten phase:

$$\frac{L_v}{T_{boiling}} \approx 85 - 88\frac{J}{Kmol} \tag{21}$$

In this work, the boiling temperature of the molten phase has been taken as that of Levoglucosan (384 °C) [40]. Gas radiation is

Table 2
Devolatilization kinetics parameters.

Parameter	Unit	Constant	References
Small size fractions (<112 µm): High-temperature kinetics, one-step reaction mechanism			
A_1	s^{-1}	8.56×10^{10}	[16]
Ea_1	KJ•mol^{-1}	171.8	
Medium size fractions (112–616 µm): High-temperature kinetics, one-step reaction mechanism			
A_2	s^{-1}	3.99×10^{9}	[16]
Ea_2	KJ•mol^{-1}	162.3	
Large size fractions (616–2000 µm): High-temperature kinetics, one-step reaction mechanism			
A_3	s^{-1}	2.62×10^{6}	[16]
Ea_3	KJ•mol^{-1}	118.7	
Kinetic parameters for the two-step reaction mechanism, valid for low heating rates.			
A_V	s^{-1}	1.11×10^{11}	[41]
Ea_V	KJ•mol^{-1}	177	
A_T	s^{-1}	9.28×10^{9}	[41]
Ea_T	KJ•mol^{-1}	149	
$A_{V,2}$	s^{-1}	4.28×10^{6}	[42]
$Ea_{V,2}$	KJ•mol^{-1}	108	

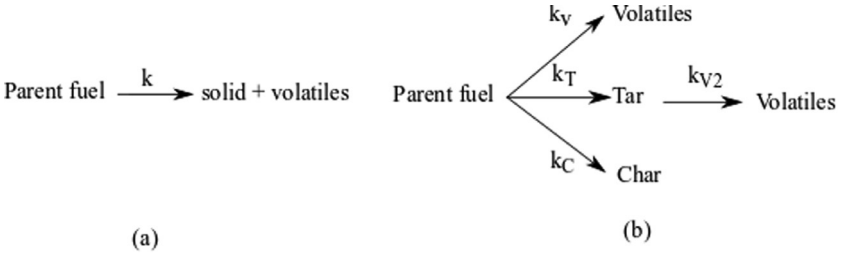

Fig. 6. Reaction models (a) One-step reaction mechanism, used at high temperatures and heating rates (b) Two-step reaction mechanism, based on the Broido-Shafizadeh scheme, valid for low heating rates and lower temperatures.

especially important in environments with high partial pressures of radiating gases (CO_2 and H_2O) and can be obtained from the Hottel correlations for mixtures of CO_2 and H_2O, corrected for mutual radiation [41]. Back-radiation from incandescent particles and sooty clouds can be disregarded under very dilute flows, although they can contribute to maintaining particle temperature. Particle emissivity was assumed as 0.3 [42]. Finally, the energy exchange by radiation between gas and particles can be obtained from:

$$E_r = -\sigma_{sb}\left(\varepsilon_g T_g^4 - \varepsilon_p \alpha_g T_p^4\right) \tag{22}$$

where E_r is the energy transferred to the particle by radiation.

The estimated temperature from the energy balance for each experimental point is used to determine the kinetic coefficients of a devolatilization model in order to calculate the conversion. The biomass particles during the devolatilization stage under industrially realistic conditions for suspension firing is non-isothermal. Therefore, it is necessary to consider a non-isothermal correction and the use of kinetic parameters optimized for high temperatures and heating. The kinetic parameters for a zero-dimensional, single first-order reaction (0D SFOR) model (Fig. 6a) by Johanssen et al. [16] were used in this study. Kinetic parameters were optimized with the results of an experimentally validated model for single particles, where local conversion is solved over particle radius, and intermediate species are considered using the reaction model of Fig. 6b. Kinetic parameters are provided for three different size fractions: small (below 100 µm), medium (100 to 600 µm), and big (above 600 µm) particles, as shown in Table 2.

Particle temperature and conversion products are calculated numerically using the Runge-Kutta method. Char gasification reactions have not been included to avoid making further assumptions since the aim of the article is to study devolatilisation reactions. This assumption seems safe, since gasification reactions have a much higher characteristic time than pyrolysis for the studied cases: $\frac{t_{pyrolisis}}{t_{gasification}} \approx 10^3 - 10^4$ for particle sizes from 50 to 1000 µm

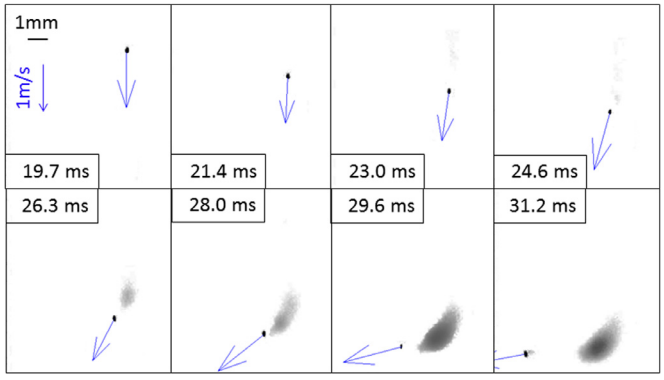

Fig. 7. Sequence of images of a particle (black) exhibiting the jet effect caused by the sudden release of volatile matter (grey area). Arrows represent particle velocity and its length correlates to velocity magnitude, indicated with the reference vector in the upper left image.

[43]. Oxidation reactions are very unlikely since the atmosphere around the particles is heavily reducing due to the fuel-rich combustion products from the flat flame. No assumptions on homogeneous chemistry have been made since only devolatilisation is considered, and it would exceed the assumptions for this article.

3. Results and discussions

3.1. Introduction to the "Rocketing" phenomenon

Figure 7 illustrates the aforementioned "rocketing" phenomenon with a sequence of images of a biomass particle undergoing devolatilization. The particle velocity vectors that are superimposed on the images have been determined with PTV and indicate the velocity magnitude. The raw images have been inverted to enhance contrast, and thus, all radiating matter in the visible

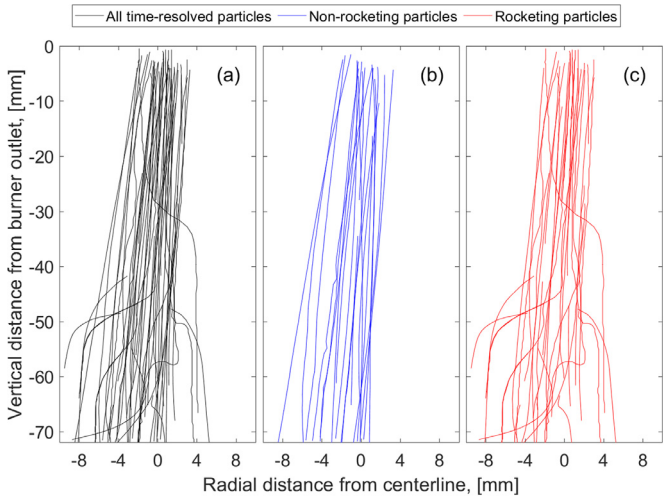

Fig. 8. Particle trajectories for: (a) all time-resolved particles (b) "non-rocketing" particles (c) "rocketing" particles.

spectra appears darker than the background. The timestep on top of the images indicates the residence time of the particle from its entrance to the reactor. The particle exhibited lateral motion in a similar manner to that of a rocket, apparently caused by a fast release of volatile matter. This phenomenon began after 23.0 ms of residence time for this particle, when a small cloud of incandescent matter emerged behind the particle. The appearance of this cloud was accompanied by a sudden deflection of the particle trajectory in the opposite direction to the release of volatiles. Judging by the wedge shape of the volatile cloud near the particle, the release of volatiles seemed to come from a narrow gap at the surface of the particle. This effect, which we refer to as "rocketing", has been observed repeatedly, for a significant fraction of the particles, in all the experiments performed for this work. The direction of the deflection was random, sometimes directing the particle upstream. The residence time at which the phenomenon took place varied from particle to particle.

3.2. The collective behaviour of "rocketing" versus "non-rocketing" particles

3.2.1. Categorization of behaviour and parametric analysis

The "rocketing" phenomenon was easily recognizable from direct observation of the time-resolved particle trajectories and comparison with the recorded experimental images, as it was seen in Section 3.1. However, not all the detected particles remained within the thickness of the laser sheet, and the trajectories were rarely complete. Therefore, velocity and properties of "rocketing" and "non-rocketing" particles have been extracted from a statistically significant number of particles, which remained within the laser sheet throughout the field of view. Then, these properties have been averaged at each residence time for each category. Fig. 8 presents the trajectories for the particles which remained within the thickness of the laser sheet along the field of view. Trajectories in red and blue correspond to "rocketing and "non-rocketing" particles, respectively. Within the ones exhibiting "rocketing", it is possible to see large motion deflections, presumably due to the ejection of a narrow jet of gas from the particle surface that gives rise to a net thrust. It can be also noted that there is migration towards negative radii for all trajectories. This can be explained by the non-axysimmetry of the gas flow, caused by a misalignment in the carrier gas injection line. Flow inhomogeneities causing lift can be disregarded, as it is further discussed in section 3.3.2 of this manuscript. Further discussion on this topic can be found in Section 4 of the supplementary material.

Figure 9 depicts time-averaged properties for "rocketing" and "non-rocketing" particles, namely: acceleration (Fig. 9a), slip velocity (Fig. 9b), particle velocity (Fig. 9c), and particle dimensions (Fig. 9d to f), including volume, minimum diameter and aspect ratio. Continuous lines represent mean values, and shaded areas indicate standard deviation around the mean. Graphs with the raw data used for these graphs can be found in the supplementary material (Figure S1).

Figure 9a represents average acceleration versus residence time and reveals intense fluctuations in the acceleration of "rocketing" particles. Meanwhile, the average acceleration of "non-rocketing" particles changed smoothly with a small standard deviation. These fluctuations are caused by the sudden accelerations accompanying the "rocketing" phenomenon. The average acceleration of all trajectories at the entrance to the reactor was slightly lower than the acceleration of gravity and with higher dispersion for the "rocketing" particles. This could be attributed to the smaller size of the "rocketing" particles, therefore presenting less gravimetric force, as it is discussed in further sections.

Figure 9b represents average slip velocity as a function of residence time. Average slip velocity at the entrance to the reactor was very similar and had an analogous standard deviation for both categories of particles. As residence time increased, the average slip velocity for "rocketing" particles tended towards zero, indicating that "rocketing" particles were entrained in the gas flow faster than the "non-rocketing" ones. The differences in average slip velocities between "rocketing" and "non-rocketing" particles started appearing after approximately 20 ms of residence time.

Figure 9c represents average particle velocity versus residence time. Here, it can be seen that the "rocketing" particles travelled at a significantly lower velocity, compared to the "non-rocketing" ones, already from the entrance of the reactor. This interesting result indicates that, from a time-averaged perspective, the tendency towards particle entrainment in the gas flow is a more relevant factor to represent the motion of the "rocketing" particles, rather than the short but intense velocity fluctuations that help identify it.

Regarding morphology presented in Fig. 9d–f, particles that exhibited "rocketing" motions were on average slightly smaller and consistently less elongated when they entered the reactor. During conversion, intense shrinking was noticeable for both "rocketing" and "non-rocketing" particles. Additionally, later entrainment of "rocketing" particles in the gas flow was accompanied by spheroidization. This is indicated by a decrease in particle aspect ratio and a simultaneous increase of the minimum diameter. It is unknown whether "non-rocketing" particles also tended to spheroidize, since they did not remain long enough within the field of view.

As summarized above, already at the entrance to the reactor, the "rocketing" particles were smaller, rounder and travelled on average slower than the "non-rocketing" counterparts. This result has been used to develop a predictive model of the "rocketing" effect based on the original size and shape of the feedstock, which can be found in subsequent sections. Moreover, as conversion proceeded, "rocketing" particles got entrained in the gas flow as they shrank and spheroidized. In contrast, for "non-rocketing" particles, gas flow entrainment did not happen within the field of view of the camera. Therefore, from a time-averaged perspective, the "rocketing" phenomenon affects the response time of the particles in a fluid, allowing them to get entrained faster in the gas flow.

3.2.2. Frequency of "rocketing"

Results from Section 3.2.1. indicate that particles exhibiting the "rocketing" effect had a smaller minimum diameter and a lower

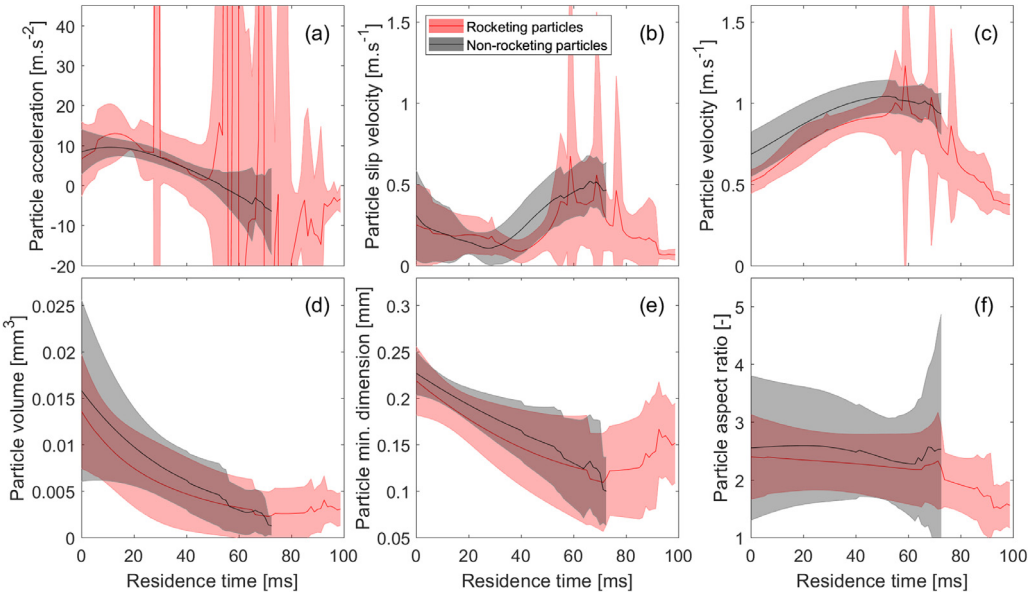

Fig. 9. Time-averaged properties of "rocketing" and "non-rocketing" trajectories.

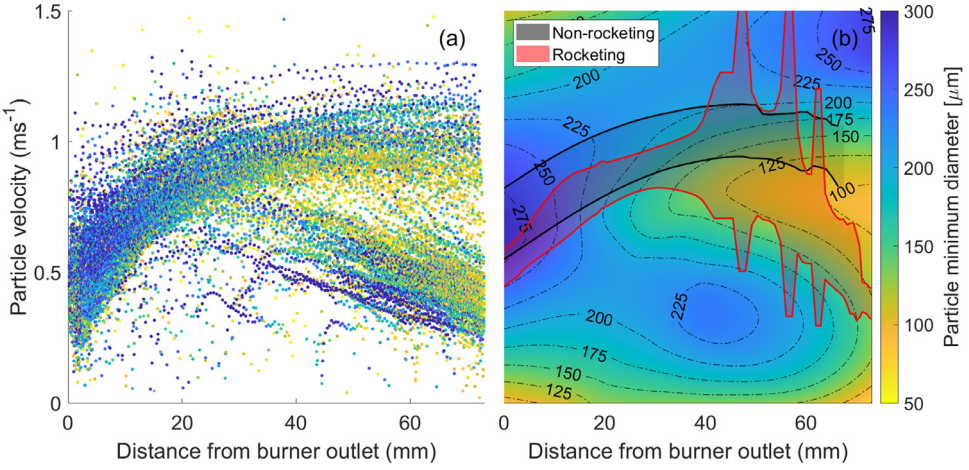

Fig. 10. (a) Scatter plot of with all particles detected in the experiment, colorscale based on minimum diameter (b) Projection of a Loess fit of the points defined by velocity, distance from burner outlet and minimum diameter. Overlayed on top of this graph: data from Fig. 9c.

aspect ratio than the non-rocketing ones. The results from the averaged properties of these trajectories can only represent qualitatively the differences between each behaviour. To draw quantitative information on the differences between behaviours, it is necessary to analyse a larger number of particles, using a time-averaged approach. However, not all particles could be followed for the entire field-of-view due to: (1) out-of-plane motions (see Section 6 of the supplementary material), (2) hindered particle recognition in regions with high light intensity, (3) particles moving close to each other causing failure in track reconstruction and (4) the sudden motions of "rocketing" particles preventing track reconstruction. Instead, all samples detected from the experiment have been taken into account, including all repeated samples from each particle.

Figure 10 shows (a) the scatter plot with all samples detected during the experiment, with the colour scale indicating particle size, and (b) the 2D projection of the surface fit for the *z*-axis. Overlayed on top of graph (b), the averages of time-resolved particle velocity versus distance from the burner outlet for "rocketing" and "non-rocketing" behaviours can be found. To allow comparison with qualitative time-resolved data from section 3.2.1, velocity contours for averaged time-resolved data from Fig. 9 have been integrated to be represented against distance from the burner outlet.

The scatter plot in Fig. 10a shows two distinct velocity behaviours diverging from 20 mm from the burner outlet. Figure 10b indicates that the upper branch corresponds to the behaviour of "non-rocketing" particles, while the lower branch corresponds to the "rocketing" ones. A significant amount of samples were detected during the experiment exhibiting the "rocketing" phenomenon. Therefore, the particles belonging to these samples were responsible for the discrepancies with our previous simulation work [27] due to their tendency towards getting entrained in the gas flow. Further information can be found in Section 7 of the supplementary material.

The clear velocity branching caused by "rocketing" particles, seen after 20 mm from the burner outlet in the scatter plot of Fig. 10a, and the high number of detected samples throughout the experiment, allows a statistically significant quantification of the frequency of the two behaviours. The categorization has been done by histograms of normalized particle velocity from 0 **to** 5 mm from the burner outlet and from 40 to 45 mm from the burner outlet. All velocities used for these histograms were translated to the ini-

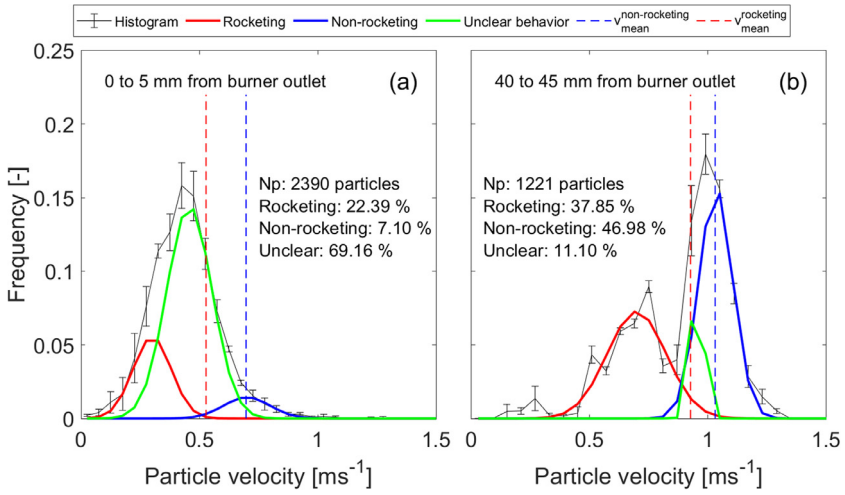

Fig. 11. Histograms and tri-normal fits of particle velocity at (a) 0–5 mm from the burner outlet and (b) 40–45 mm from the burner outlet. Dashed lines indicate average velocity from time-resolved measurements at the beginning of each range of distances from the burner outlet. Np stands for number of particles.

tial value of the range. To avoid the inclusion of repeated measurements of the same particle trajectory in the frequency analysis, multiple histograms were obtained and averaged for the minimum displacement possible, given the velocities observed. Fig. 11 represents the histograms of particle velocity for 5 mm below the burner outlet and 40 to 45 mm below the burner outlet. The velocity obtained from the limited number of the complete trajectory (section 3.2.1) is also represented with dashed lines. The histogram of velocities at 40–45 mm from the burner outlet presented a bimodal distribution. To estimate the frequency of the "rocketing" effect with the consideration of the overlap between the two modes, the histogram was deconvoluted to a trinomial distribution, forcing the modes to be the closest to the average time-resolved velocities while maximizing the R^2. The areas under these curves were used to obtain the fractions of "rocketing", "non-rocketing", and particles with unclear behaviour due to overlap. The trinomial distribution was fit to the histogram data using the "fit" function with a fitting equation in Matlab. An iterative seek was performed so as two Gaussians had means as close as possible to the average time-resolved velocities while maximising the R^2. This was made by changing the options for the Matlab fitting function (upper and lower limits of the function "fit"). No other thresholds were used. The resulting Gaussians were classified into "rocketing", "unclear" and "non-rocketing" based on their distances to the average time-resolved velocities.

As it can be seen from the data presented in Fig. 11, at around 40–45 mm from the burner outlet, the percentage of "rocketing" particles was at least 37%. Many of these particles also exhibited an intense deceleration, as it can be attested by comparing the average time-resolved velocity. The bimodal distribution from 0 **to** 5 mm from the burner outlet does not allow enough accuracy for quantifying the frequency of the "rocketing" phenomena, given the number of unclear particles. However, the fitted distributions of "rocketing" and "non-rocketing" particles are sufficiently separated from each other to assign probabilities of "rocketing" based on particle velocity. Probability plots can be found in the supplementary material.

The probability of "rocketing", obtained from Fig. 11a, was expressed as a function of minimum diameter and aspect ratio for all the particles used for the histogram in Fig. 11a. The same translation to coincide with the initial value of the range was performed in the same way as with velocities for the previous histograms. The function was expressed as the sum of two logistic regressions. Figure 12 represents the results of this estimation, indicating that for a spherical particle with 200 µm of diameter, the probability of rocketing is approximately $p \approx 20+15=35\%$. More information on the surface fit can be seen in the supplementary material.

3.2.3. Discrepancies between the estimated and measured velocity at the entrance to the reactor

The cause for the different velocities at the entrance to the reactor for "rocketing" and "non-rocketing" particles is intriguing. It must be examined whether it can be explained solely based on size and shape differences or if other phenomena such as additional forces could be involved. This study must consider the sharp temperature gradient at the entrance to the reactor, which will affect drag forces in its immediate surroundings. For this, the velocity of the particles from the feeding mechanism, through the conveying tube until the entrance to the reactor ($y=0$), has been estimated from the geometrical data, carrier gas velocity and temperature profile, assuming only drag and weight as the only forces acting on the particles.

Figure 13a represents the drag force to weight ratio before and after entering the reactor from the feeding tube. It indicates a drastic reduction of the drag force compared to the weight upon the injection from the feeding line to the burner. It was caused by the change in carrier gas properties while heating up. Therefore, weight was most probably the main contributing force to momentum at the entrance to the reactor, which explains why the average acceleration of the particles at the entrance to the reactor was close to gravity. Fig. 13b shows the comparison between estimated particle velocity and measured one at the origin of coordinates. Calculation of the balance between drag and weight fails to predict the velocity of "rocketing" particles at the entrance of the reactor based on their size and shape.

Potential reasons for this discrepancy are either: (1) drag force is greatly underestimated or (2) an additional force or phenomenon is present. Given the intense changes in temperature and gas properties, this discrepancy could be explained by the effect of devolatilization products, such as changes in the gas properties or the momentum exchange between volatiles, gas and particles during conversion. Scenario (1) is not very plausible since most models correcting for Stefan flow (gas emanating from the surface of the particle) predict a lubricating layer around the particle, causing a decrease in the drag coefficient and, therefore, the drag force [44]. Only one model predicts an increase in the drag force due to Stefan flow, but it is expected to occur under combustion [45]. For scenario (2), additional forces such as those described in the theory section could be related to this phenomenon. Subsequent sections will investigate the estimated forces on two

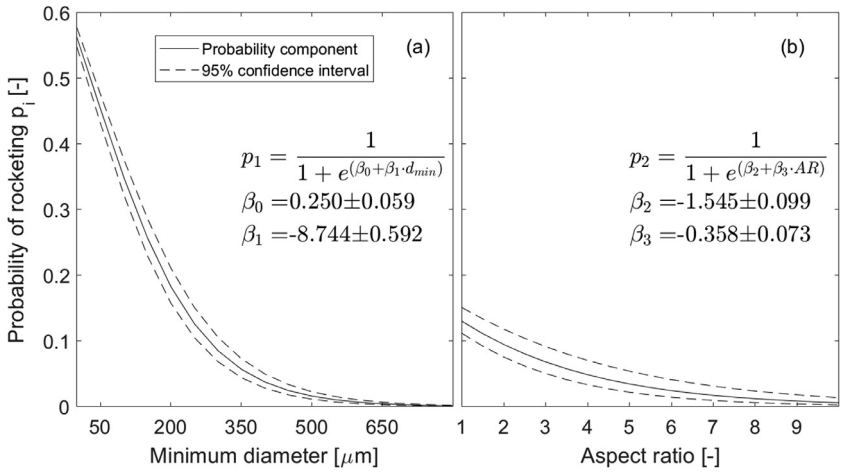

Fig. 12. Stochastic model for "rocketing" probability as a function of (a) Minimum diameter and (b) aspect ratio.

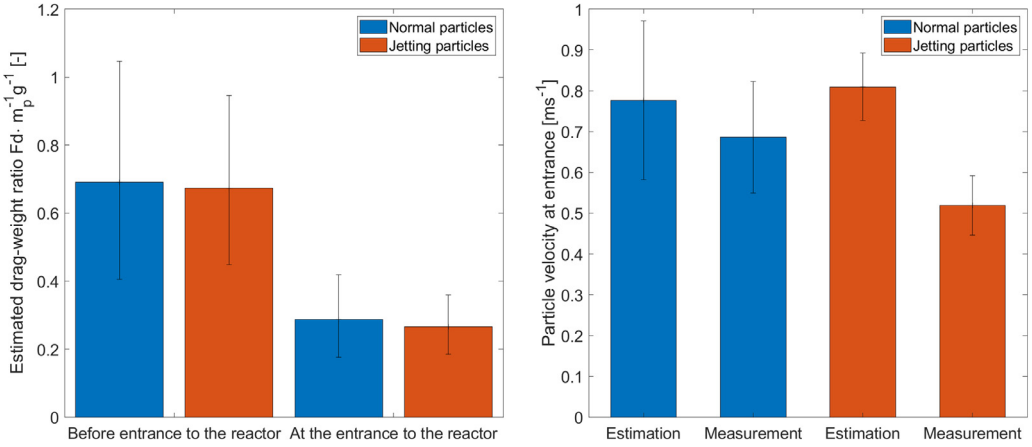

Fig. 13. (a) Estimated drag-weight ratio before and after entering the reactor (b) Estimated versus measured particle velocity at the entrance to the reactor. For the measured values, errorbars indicate standard deviation. For the estimation, errorbars indicate the minimum and maximum values obtained taking into account the dispersion of the raw data.

particles exhibiting "rocketing" and "non-rocketing" phenomena and try to distinguish which force could be related to such an event.

3.3. Behaviour of individual "rocketing" particles

3.3.1. Particle motion of a "rocketing" and a "non-rocketing" particle

Two particles have been chosen as representative examples of the "rocketing" and "non-rocketing" behaviours. Fig. 14 contains a series of snapshots of these two particles at different residence times. In these images, particles always appear white due to the scattered light from the laser. Therefore their pixel intensity is not related to temperature. As devolatilization proceeds, volatile matter is released, which eventually becomes incandescent and appears in the images as diffused grey areas. The pixel intensity of these clouds is a combination of Mie scattering and radiation in the visible spectrum. Underneath each image, it is indicated whether the particles were accelerating, "rocketing", or decelerating. Their behaviour is identified as "rocketing" and "non-rocketing". At their entrance into the reactor, the "non-rocketing" particle was substantially more elongated and bigger in volume than the "rocketing" one. For the "rocketing" particle, the cloud of incandescent volatiles appeared at around 15 ms (not included in the set of images). This cloud followed the particle as it moved downstream, stretching vertically. After 40 ms, the particle began to escape the cloud in the direction of gravity, "rocketing" violently out of it at around 54 ms. The particle can be seen escaping the cloud of volatiles from the bottom in the image at 63.8 ms. After rocketing, the particle moved downstream without a visible cloud of volatile gases surrounding it and appeared slightly swollen compared to the size during rocketing. For the "non-rocketing" particle, the cloud of incandescent volatiles also appeared at around 15 ms. However, it was less intense (figure not included in this set of images), either from volatiles being released in lesser amounts or by being at a colder temperature. The cloud of the "non-rocketing" particle achieved its maximum size at around 40 ms. Eventually, similar to the "rocketing" particle, the "non-rocketing" one also escaped the cloud of volatiles and did not show more signs of a cloud around it.

Figure 15 shows the particle velocity and effective velocity against residence time for these two particles. Coloured backgrounds indicate deceleration, acceleration and "rocketing" stages, and average acceleration during these stages is characterised by text on the graph. For the particle velocity plots, a piecewise polynomial fit with 95% confidence intervals is added to the graph for easier interpretation of the results. Additionally, the gas velocity measured without particles is included after being converted to the particle frame of reference. For the effective velocity, there is a lack of experimental points before 15 ms of residence time for the "rocketing" particle. These points have been obtained by linear extrapolation of subsequent data and are indicated in the plot by dashed lines.

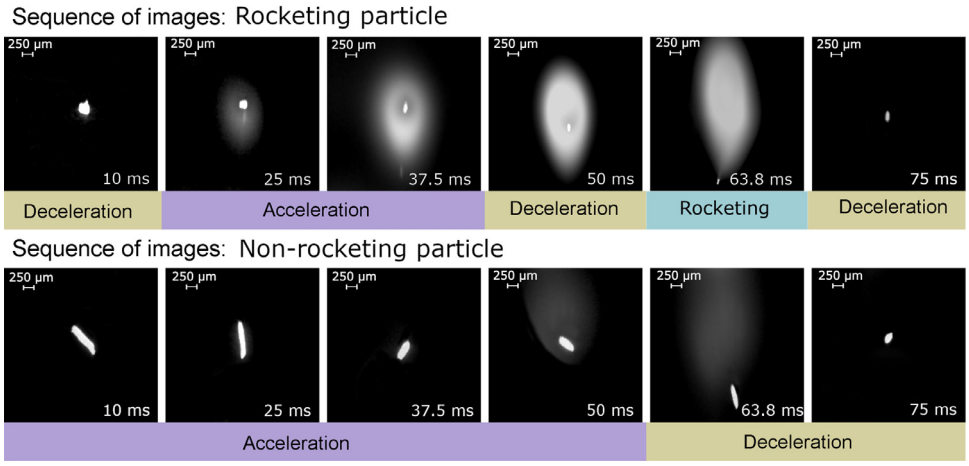

Fig. 14. Snapshots of the particles studied during the different stages.

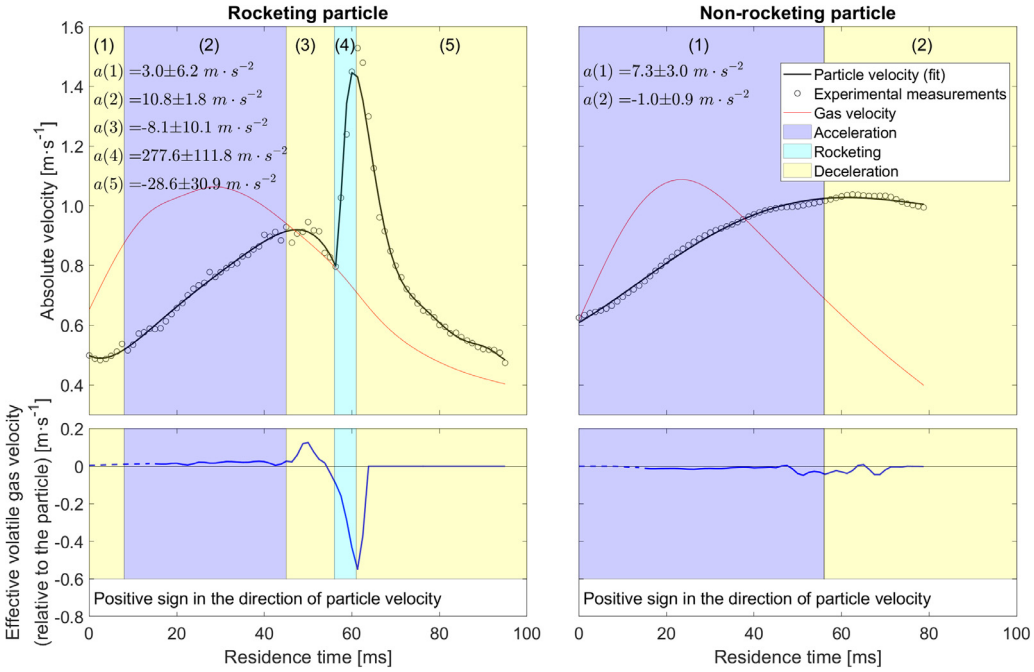

Fig. 15. Different stages of particle motion for a rocketing and a non-rocketing particle. The particle velocity is positive for motion in the direction of gravity.

The "rocketing" particle decelerated immediately after entering the reactor. Given that gas and particle are in co-flow, it would be expected that the gas aided particle motion at the entrance. Such deceleration could also be attributed to thrusting due to drying, starting near the burner outlet. The effective velocity of these gases would not be detected by the method previously explained since it requires an incandescent cloud of volatiles.

Afterwards, the particle continued almost at free fall. A possible explanation for this is the presence of the Stefan flow from the particle surface due to devolatilization. This could have caused drag reduction by creating a thickened lubricating layer, and if the Stefan flow is heterogeneous, thrust/drag compensation. Both possibilities are plausible since there is a small effective velocity present during this stage, as can be seen in Fig. 15. Eventually, "rocketing" was observed with a sudden increase in the magnitude of acceleration, explained by the thrust caused by the release of volatile gases.

Later on, the "rocketing" particle decelerated suddenly and followed the stream of gas. By contrast, the "non-rocketing" particle decelerated only slightly towards the end of its trajectory. The "Rocketing" particle was accompanied by a noticeable increase in the effective velocity, which caused a net thrust force. Interestingly, in the case of this specific particle, thrust initially opposed the particle's motion, due to volatiles being released in the same direction as particle velocity, temporarily slowing it down. After this, the direction of the effective velocity quickly changed, and the particle was propelled diagonally. This indicates that for sufficiently high effective velocities, the particle could have been propelled upstream. Particle rotation can explain the general tendency of particles for being propelled diagonally. By contrast, the effective velocity observed in the "non-rocketing" particle is substantially lower.

3.3.2. Estimated mass loss during "rocketing" from estimated forces

Figure 16 presents the estimated particle mass during conversion for the same "rocketing" particle from Section 3.3.1. A sensitivity analysis to the model applied in this section, and an uncertainty analysis to all derived parameters can be found in Section 3 of the supplementary material. This result was obtained using the methodology described in Section 2.1. Note that the vertical axis

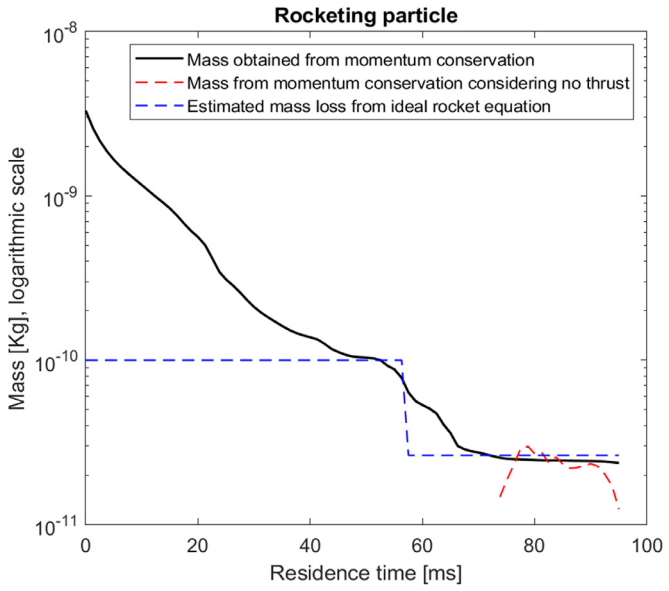

Fig. 16. Comparison of mass obtained from equilibrium of forces for a "rocketing" particle. Overlayed to this plot, the estimated mass loss required for the ideal rocket equation (blue) and the final calculated mass from experimental measurements without considering thrust force.

is on a logarithmic scale. For comparison, a graph with the estimated mass loss during rocketing, calculated using the ideal rocket equation from Section 2.1.4, has been overlayed with blue dashed lines. The solution to the ideal rocket equation used as initial mass is given by the estimation right before "rocketing". This is shown with blue dashed lines in Fig. 16. In addition, a direct solution of Eq. (4) without thrust force has been obtained after rocketing (represented with red dashed lines). This was done to check whether particle motion after rocketing could be explained without the need for a thrust force.

Figure 16 indicates that the mass of the particle during the rocketing phenomenon is very small compared to its original value at the entrance. Therefore, the "rocketing" phenomenon took place for this particle at an advanced stage of conversion where the mass of the particle had lost more than 90% of its original value. However, during "rocketing", the particle loses 80% of the remaining mass while being quickly propelled away. Fig. 16 also indicates that the ideal rocket assumption is in agreement with the increase of momentum experienced by the particle due to the amount of mass released and that no more thrust needed to be assumed after rocketing for the estimation of the particle mass.

Figure 17 shows the forces on the particle during conversion that were obtained from the solution for the mass, using the methodology presented in Section 2.1. The initial deceleration requires an initial thrust force on the "rocketing" particle. This force would be present even at very small effective velocities, and it is almost not present for the "non-rocketing" particle. Thrust force also explains the sudden acceleration during the "rocketing" effect. Other forces, such as Saffman and Basset force are relevant only when the slip velocity becomes zero. Although these forces are irrelevant during most of the residence time, they might become important to avoid integration errors from the solution of Eq. (4), due to the instantaneous zero value of the drag force at the zero-crossing. However, they cannot be the only cause for the sudden lateral displacements or the lateral deviation of the trajectories.

The rocketing particle began thrusting towards its windward side when slip velocity was already low, decelerating the particle to the point of almost zero drag before eventually being propelled diagonally. Once the particle begins to gain velocity due to its increased momentum, drag increases again, slowing down the particle.

3.3.3. Estimated particle temperature, composition and density during "rocketing" for different devolatilization models

Figure 18 shows the calculated mass and temperature using the methodology from Section 2.2. for the same "rocketing" and "non-rocketing" particles studied in Section 3.3.1 and 3.3.2. A sensitivity analysis of the model used in this section and an uncertainty analysis to all derived parameters can be found in Section 3 of the supplementary material. Apparent devolatilization kinetics for small particles agrees best with the "rocketing" particle, while conversion of the "non-rocketing" one is better approximated by the kinetics model for medium particle size. Particle temperature estimations using the kinetics model for small particles show a much faster rise than other models and follow gas temperature.

Figure 19 represents the estimated yield of products and particle density for the "rocketing" and "non-rocketing" particles. These were obtained using the kinetic models that agree best with the mass in Fig. 18. Modelling results of product yield and density shown in Fig. 19 indicate that most of the mass was lost at a more or less constant density initially. This result is in accordance with Holmgren et al. [46]. During the subsequent "rocketing" stage, the "rocketing" particle became very dense and turned fluffy (with very low density) after thrusting. Rocketing could be possible due to some unconverted material or gas trapped in the particle's core due to the non-isothermal heating or by bubble formation caused

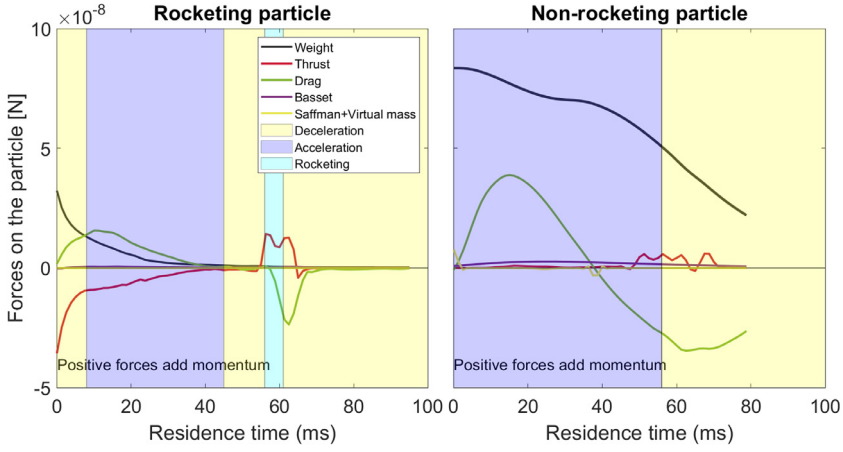

Fig. 17. Estimated forces on the particles. Background colours indicate the regions of acceleration, deceleration and rocketing.

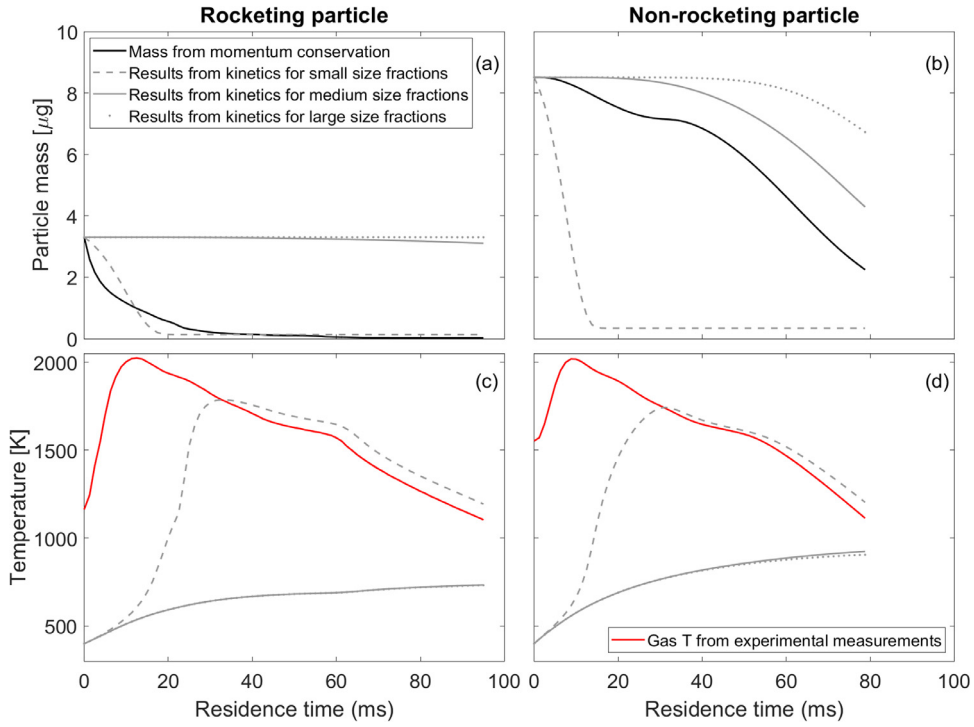

Fig. 18. From left to right and top to bottom: (a,b) Estimated mass from equilibrium of forces and thermochemical models for a "rocketing" and "non-rocketing" particle (c,d) Estimated particle and gas temperature from thermochemical models and experimental measurements, respectively.

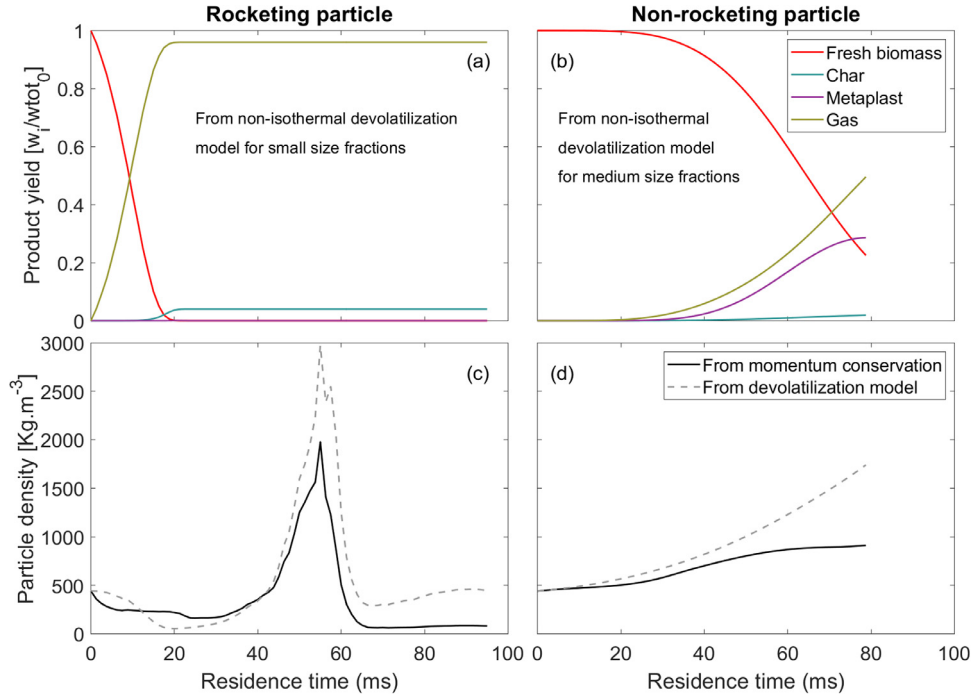

Fig. 19. From left to right and top to bottom: (a,b) Estimated yield of devolatilization products, using the models best fitting to particle conversion (c,d) Estimated particle density from kinetic models and balance of forces.

by a metaplastic stage. However, the latter is hard to predict with the available kinetic parameters for metaplast formation, which have been measured at much slower heating rates. The product composition shown in Fig. 19 does not indicate any yield of metaplast for the "rocketing" particle. However, the modelling results for the "non-rocketing" particle indicated a significant formation of metaplast.

3. Conclusions

This study provides experimental evidence of the sudden acceleration of fuel particles, referred to as "rocketing", during biomass devolatilization. The feedstock studied was Norwegian Spruce particles under suspension firing conditions, with an atmosphere similar to that encountered under entrained flow gasification. The

"Rocketing" phenomenon takes place at a high degree of conversion, and it is probably caused by gas trapped inside a highly dense particle, which likely underwent a metaplastic stage. "Rocketing" particles presented faster apparent devolatilization kinetics than the "non-rocketing" ones.

Particles exhibiting "rocketing" phenomena were frequent within the stream of devolatilization particles, with around 37% of the particles exhibiting this effect. This has important implications for the time-averaged velocity of the stream of particles since particles showing the "rocketing" effect turn fluffy and spherical after "rocketing", and have a higher tendency to get entrained in the gas flow.

The probability of exhibiting "rocketing" phenomena during conversion is related to the size and aspect ratio of the original feedstock. This work provides a simple statistical model for its prediction under the studied conditions, which can be easily implemented as a stochastic model in CFD simulations.

Estimation of forces based on theoretical modelling using experimental results indicates that, under the experimental conditions studied here, a drag force calculated with the Schiller-Naumann correlation with Clift's correction for spheroid particles can explain the transient motion of "non-rocketing" particles. However, for particles exhibiting the "rocketing" effect, these estimations alone cannot explain the transient motion of these particles, and this discrepancy is presumably related to the presence of an additional thrust force caused by directional blowing during fast devolatilization.

Declaration of Competing Interest

The authors declare that they have no known competing financial interests or personal relationships that could have appeared to influence the work reported in this paper.

Acknowledgements

The authors would like to thank the national strategic research environment, Bio4Energy, the Swedish Energy Agency, and the industrial consortium through Swedish Centre for Biomass Gasification (SFC) as well as the Research Council of Norway through GASPRO (No. 267916) for the financial support. Kempe Foundation is greatly acknowledged for the financial support for the experimental facility.

Supplementary materials

Supplementary material associated with this article can be found, in the online version, at doi:10.1016/j.combustflame.2021.111898.

References

[1] F. Cherubini, G.P. Peters, T. Berntsen, A.H. Strømman, E. Hertwich, CO_2 emissions from biomass combustion for bioenergy: atmospheric decay and contribution to global warming, GCB Bioenergy 3 (2011) 413–426.
[2] J. Hansen, M. Sato, P. Kharecha, D. Beerling, R. Berner, Target atmospheric CO_2: where should humanity aim? Open Atmos. Sci. J. 2 (2008) 217–231.
[3] S.N. Naik, V.V. Goud, P.K. Rout, A.K. Dalai, Production of first and second generation biofuels: a comprehensive review, Renew. Sustain. Energy Rev. 14 (2010) 578–597.
[4] K. Qin, Entrained Flow Gasification of Biomass, Technical University of Denmark, Lyngby, Denmark, 2012.
[5] T. Wall, Y. Liu, C. Spero, L. Elliott, S. Khare, R. Rathnam, et al., An overview on oxyfuel coal combustion-State of the art research and technology development, Chem. Eng. Res. Des. 87 (2009) 1003–1016.
[6] A. Molino, S. Chianese, D. Musmarra, Biomass gasification technology: the state of the art overview, J. Energy Chem. 25 (2016) 10–25.
[7] B. Göktepe, Entrained Flow Gasification of Biomass: Soot Formation and Flame Stability, Luleå University of Technology, Luleå, Sweden, 2015.
[8] T. Milne, R.J. Evans, Biomass Gasifier " Tars ": Their Nature, Formation, and Conversion, National Renewable Energy Laboratory, Golden, Colorado, USA, 1998 Report No. NREL/TP-570-25357.
[9] J.M. Johansen, R. Gadsbøll, J. Thomsen, P.A. Jensen, P. Glarborg, P. Ek, et al., Devolatilization kinetics of woody biomass at short residence times and high heating rates and peak temperatures, Appl. Energy 162 (2016) 245–256.
[10] H. Lu, Experimental and Modeling Investigations of Biomass Particle Combustion, Brigham Young University, Provo, USA, 2006.
[11] Colomba Di Blasi, Modeling chemical and physical processes of wood and biomass pyrolysis, Prog. Energy Combust. Sci. 34 (2008) 47–90.
[12] M. Van de Velden, J. Baeyens, A. Brems, B. Janssens, R. Dewil, Fundamentals, kinetics and endothermicity of the biomass pyrolysis reaction, Renew. Energy 35 (2010) 232–242.
[13] A.M.C. Janse, R.W.J. Westerhout, W. Prins, Modelling of flash pyrolysis of a single wood particle, Chem. Eng. Process. Process Intensif. 39 (2000) 239–252.
[14] C. Blasi, Heat, momentum and mass transport through a shrinking biomass particle exposed to thermal radiation, Chem. Eng. Sci. 51 (1996) 1121–1132.
[15] J.M. Johansen, P.A. Jensen, P. Glarborg, N. De Martini, P. Ek, R.E. Mitchell, High heating rate devolatilization kinetics of pulverized biomass fuels, Energy Fuels 32 (2018) 12955–12961.
[16] J.M. Johansen, P.A. Jensen, P. Glarborg, M. Mancini, R. Weber, R.E. Mitchell, Extension of apparent devolatilization kinetics from thermally thin to thermally thick particles in zero dimensions for woody biomass, Energy 95 (2016) 279–290.
[17] M.C. Yuen, L.W. Chen, On drag of evaporating liquid droplets, Combust. Sci. Technol. 14 (1976) 147–154.
[18] A. Elfasakhany, L. Tao, B. Espenas, J. Larfeldt, X.S. Bai, Pulverised wood combustion in a vertical furnace : experimental and computational analyses, Appl. Energy 112 (2013) 454–464.
[19] C. Brackmann, M. Aldén, P.E. Bengtsson, K.O. Davidsson, J.B.C. Pettersson, Optical and mass spectrometric study of the pyrolysis gas of wood particles, Appl. Spectrosc. 57 (2003) 216–222.
[20] N. Guo, T. Li, L. Zhao, T. Løvås, Eulerian-Lagrangian simulation of pulverized biomass jet using spheroidal particle approximation, Fuel 239 (2019) 636–651.
[21] A.R. Teixeira, K.G. Mooney, J.S. Kruger, C.L. Williams, W.J. Suszynski, L.D. Schmidt, et al., Aerosol generation by reactive boiling ejection of molten cellulose, Energy Environ. Sci. 4 (2011) 4306–4321.
[22] J. Montoya, B. Pecha, F.C. Janna, M. Garcia-Perez, Single particle model for biomass pyrolysis with bubble formation dynamics inside the liquid intermediate and its contribution to aerosol formation by thermal ejection, J. Anal. Appl. Pyrolysis 124 (2017) 204–218.
[23] A.G. Borrego, L. Garavaglia, W.D. Kalkreuth, Characteristics of high heating rate biomass chars prepared under N_2 and CO_2 atmospheres, Int. J. Coal Geol. 77 (2009) 409–415.
[24] K. Umeki, K. Kirtania, L. Chen, S. Bhattacharya, Fuel particle conversion of pulverized biomass during pyrolysis in an entrained flow reactor, Ind. Eng. Chem. Res. 51 (2012) 13973–13979.
[25] T. Li, M. Geier, L. Wang, X. Ku, B. Matas, T. Løvås, et al., Effect of torrefaction on physical properties and conversion behavior of high heating rate char of forest residue 29 (2015) 177–184.
[26] J. Riaza, J. Gibbins, H. Chalmers, Ignition and combustion of single particles of coal and biomass, Fuel 202 (2017) 650–655.
[27] N. Guo, Á.D. García Llamas, T. Li, K. Umeki, R. Gebart, T. Løvås, Computational fluid dynamic simulations of thermochemical conversion of pulverized biomass in a dilute flow using spheroidal approximation, Fuel 271 (2020) 117495.
[28] Á.D. García Llamas, N. Guo, T. Li, R. Gebart, T. Løvås, K. Umeki, Morphology and volume fraction of biomass particles in a jet flow during devolatilization, Fuel 278 (2020) 118241.
[29] C.T. Crowe, J.D. Schwarzkopf, Multiphase Flows with Droplets and Particles, CRC Press, Boca Raton, USA, 2012.
[30] D.A. Khalitov, E.K. Longmire, Simultaneous two-phase PIV by two-parameter phase discrimination 32 (2002) 252–268.
[31] L.F. Shampine, M.W. Reichelt, Ode Matlab Solvers, J. Sci. Comput. 18 (1997) 1–22.
[32] J. Repola, Models for vertical wood density of scots pine, norway spruce and birch stems, and their application to determine average wood density, Silva Fenn 40 (2006) 673–685.
[33] K. Tsiolkovsky, The Exploration of Cosmic Space By Means of Reaction Devices (Исследование мировых пространств реактивными приборами), S.A. Somenova, Kaluga, Russia, 1903.
[34] E. Bar-Ziv, D.B. Jones, R.E. Spjut, D.R. Dudek, A.F. Sarofim, J.P. Longwell, Measurement of combustion kinetics of a single char particle in an electrodynamic thermogravimetric analyzer, Combust. Flame 75 (1989) 81–106.
[35] E. Biagini, S. Pintus, L. Tognotti, Characterization of high heating-rate chars from alternative fuels using an electrodynamic balance, Proc. Combust. Inst. 30 (II) (2005) 2205–2212.
[36] H. Lycksam, M. Sjödahl, P. Gren, M. Öhman, R. Gebart, High-speed interferometric measurement and visualization of the conversion of a black liquor droplet during laser heating, Opt. Lasers Eng. 50 (2012) 1654–1661.
[37] B.J. McBride, M.J. Zehe, S. Gordon, NASA Glenn Coefficients for Calculating Thermodynamic Properties of Individual Species: National Aeronautics and Space Administration, NASA/TP—2002-211556, Glenn Research Center, Cleveland, USA, 2002.

[38] M. Renksizbulut, R. Nafziger, X. Li, A mass transfer correlation for droplet evaporation in high-temperature flows, Chem. Eng. Sci. 46 (1991) 2351–2358.
[39] S. Niksa, Predicting the rapid devolatilization of diverse forms of biomass with bio-FLASHCHAIN, Proc. Combust. Inst. 28 (2000) 2727–2733.
[40] G.J. Kabo, Y.U. Paulechka, O.V. Voitkevich, A.V. Blokhin, E.N. Stepurko, S.V. Kohut, et al., Experimental and theoretical study of thermodynamic properties of levoglucosan, J. Chem. Thermodyn. 85 (2015) 101–110.
[41] B. Leckner, Spectral and Total Emissivity of Water Vapor and Carbon Dioxide, Combust. Flame 19 (1972) 33–48.
[42] P. Graeser, M. Schiemann, Char particle emissivity of two coal chars in oxy-fuel atmospheres, Fuel 183 (2016) 405–413.
[43] C. Dupont, G. Boissonnet, J.M. Seiler, P. Gauthier, D. Schweich, Study about the kinetic processes of biomass steam gasification, Fuel 86 (2007) 32–40.
[44] M.U. Thamali, R. Jayawickrama, L. Nils Erland, H. Babler, M.A. Chishty, K. Umeki, The effect of Stefan flow on the drag coefficient of spherical particles in a gas flow, Int. J. Multiph. Flow 117 (2019) 130–137.
[45] H. Zhang, K. Luo, N.E.L. Haugen, C. Mao, J. Fan, Drag force for a burning particle, Combust. Flame 217 (2020) 188–199.
[46] P. Holmgren, D.R. Wagner, A. Strandberg, R. Molinder, H. Wiinikka, K. Umeki, et al., Size, shape and density changes of biomass particles during rapid devolatilization, Fuel 206 (2017) 342–351.